Propagating waves in a monolayer of gas-fluidized rods

L. J. Daniels and D. J. Durian

Phys. Rev. E **83**, 061304 — Published 29 June 2011

DOI: 10.1103/PhysRevE.83.061304

Propagating Waves in a Monolayer of Gas-Fluidized Rods

L.J. Daniels and D.J. Durian
Department of Physics and Astronomy, University of Pennsylvania, Philadelphia, PA 19104-6396, USA

We report on an observation of propagating compression waves in a quasi-two-dimensional monolayer of apolar granular rods fluidized by an upflow of air. The collective wave speed is an order of magnitude faster than the speed of the particles. This gives rise to anomalously large number fluctuations, $\Delta N \sim N^{0.72\pm0.04}$, which are greater than ordinary number fluctuations of $N^{1/2}$. We characterize the waves by calculating the spatiotemporal power spectrum of the density. The position of observed peaks, as a function of frequency ω and wavevector k, yields a linear dispersion relationship in the long-time, long-wavelength limit and a wavespeed $c = \omega/k$. Repeating this analysis for systems at different densities and air speeds, we observe a linear increase in the wavespeed with increasing packing fraction with almost no dependence on the airflow. We also observe that the parallel and perpendicular root-mean-square speeds of the rods are identical when wave are present, but become different at low packing fractions where there are no waves. Based on this apparent exclusivity, we map out the phase behavior for the existence of waves vs speed anisotropy as a function of density and fluidizing airflow.

PACS numbers: 45.70.-n, 47.55.Lm; 87.18.Gh, 47.54.r, 05.65.b

I. INTRODUCTION

Macroscopic granular systems have been studied extensively due to their ubiquity in industrial applications as well as the ease with which they may be visualized [1–3]. Furthermore, air-fluidized grains have demonstrated a remarkable ability to serve as both a system analogous to Brownian particles [4] as well as a proxy for colloidal and molecular glasses [5, 6]. Idealized granular media consist of spherical particles whereas real systems will have both polydispersity and anisotropic particle shape. The role of particle shape is now a topic of increasing attention. Recent experiments on vibrated rods [7–11] and rods in a hopper [12] have demonstrated the great variety of phenomena – swirling, vortices, pattern formation – that arise due to particle anisotropy alone.

Individual air- or vibro-fluidized granular rods have also been observed to self-propel, in the sense of developing a greater speed along their long axis than along their short axis [13–16]. The idea of active self-propulsion has garnered great theoretical interest [17, 18] due to the potential of unifying a broad spectrum of systems over a huge range of length scales: from biological systems like bacteria [19–22], fish [23], locusts [24], birds [25, 26], to physical systems such as agitated granular materials [7, 11] and human or animal traffic [27, 28]. In this context, self-propelling at a microscopic scale gives rise to dramatic collective behavior at the macroscopic scale including the emergence of a dynamic broken-symmetry state in which all the particles move in the same spontaneously-chosen direction as a coherent flock [29–31]. These systems are also predicted to exhibit collective motion, propagating waves, and anomalously large number fluctuations [32–36]. Despite the wealth of theory and simulation, very few experiments have been conducted due to both the difficulty of tracking and analyzing biological systems as well as finding purely physical systems in which particles self-propel. Of note, giant number fluctuations were observed in a vertically-vibrated monolayer of granular rods possessing nematic order [13]. Additionally, collective behavior in the form of whorls, jets, and vortices – in which the collective motion was an order of magnitude faster than individual particle motion – has been observed in dense populations of bacteria [20].

For this paper, we extend our earlier experiments on individual and dilute systems of air-fluidized rods [16] in order to search for giant number fluctuations and collective flock-like motion. While flocking was never observed, we do find giant number fluctuations. These appear to be coupled to the unexpected existence of density waves that propagate ballistically across the system. To begin, in Section II, we introduce the apparatus and system under study. The paper will first examine a single system at fixed density of 64% packing fraction. We describe our observation of propagating compression waves in Section III. The wavespeed is an order of magnitude larger than the root-mean-square speed of the particles; this separation of timescales results in giant fluctuations in the local number density, discussed in Section IV. Lastly, in Section V, we quantify the waves by calculating the spatiotemporal power spectrum of the density and extracting a dispersion relationship for the waves. We extend the experiments by examining how the wavespeed varies with density and airflow and mapping out phase behavior.

II. EXPERIMENTAL DETAILS

We study a monolayer of right cylindrical acetal dowel rods fluidized by a sub-levitating upflow of air. The rod specifications are length 1.27 cm, diameter 0.24 cm, aspect ratio 5, and mass 0.076 g. Except when otherwise noted, we analyze a system of 1353 rods occupying a packing fraction of 64%, with a spatially and temporally

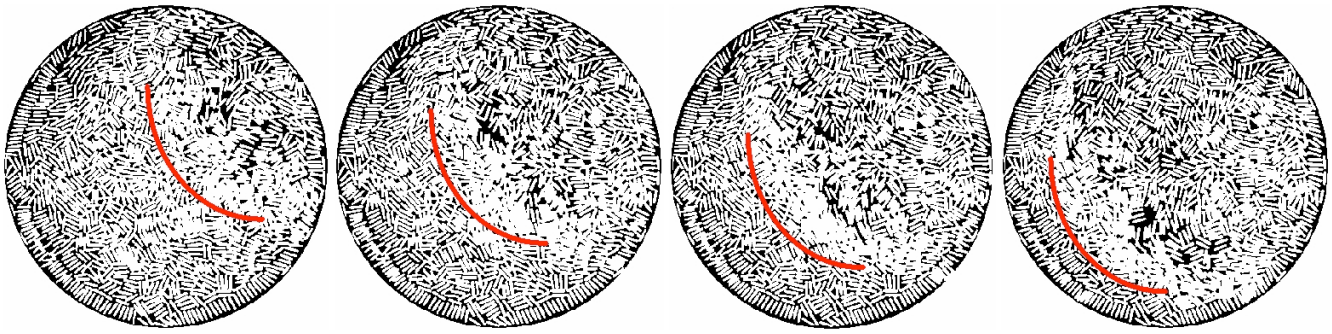

FIG. 1: (Color online) A propagating wave in a monolayer of gas-fluidized rods. The system has diameter 28.6 cm. The rods are 1.27 cm long, have an aspect ratio of five, occupy 64% projected-area packing fraction, and are fluidized by an upflow of air at 220 cm/s. The time between images, moving left to right, is 0.15 s. The solid arc ahead of the compression front is moved at a constant velocity of 28 cm/s, as a guide to the eye.

uniform upflow of air at speed 220 cm/s. This fluidizing air speed is low enough that rods do not rise or overlap out-of-plane, so that the system remains a monolayer.

The apparatus and fluidization method are identical to those of Ref. [16]. The apparatus is a rectangular windbox, $0.5 \times 0.5 \times 1.2$ m^3, positioned upright. A circular brass testing sieve with mesh size 150 μm and diameter 30.5 cm rests horizontally on top. In order to prevent particles from becoming trapped in a small groove around the edge of the sieve, we place a 1 cm norprene tube around its inside edge. A blower attached to the windbox base provides vertical airflow perpendicular to the sieve. Raw video data of the fluidized particles is captured for 10 minutes at 120 frames per second by a digital camera mounted above the apparatus. Post-processing of the video data is accomplished in LabVIEW, using the same tracking programs used in Ref. [16]. At high densities, it becomes impossible to track all the rods at all times because the bright regions of close neighbors overlap and cannot be resolved as two separate particles; nevertheless it is still possible to track enough rods for long enough to obtain speed statistics. For the analysis of the waves in Section V, we need all the rods and so abandon tracking for a direct treatment of the grayscale video data $\rho(x, y, t) \in \{0, 1, 2, \ldots, 255\}$ as a proxy for local density.

In order to emphasize the role of particle shape we analyze a companion system of 400 bidisperse plastic spheres, diameters 0.64 cm and 0.95 cm, chosen to have the same packing fraction 64% as the rod system. The air fluidization speed is 260 cm/s, chosen so that the the spheres have roughly the same rms speed as the rods. This is below the terminal falling speed, so the spheres roll without slipping or levitating.

Prior to focussing on the 1.27 cm rods with aspect ratio 5, we also explored a number of other granular rod systems. This includes apolar rods with aspect ratios of 4, 9, 14, and 30; polar rods having a distinct head and tail with aspect ratio 2.5 and 14; a range of airspeeds from 10 to 500 cm/s; and densities from 10% to 85% area packing fraction. We also examined such systems in a circular race track with width that varied from approximately three to ten particle widths, by placing a cylinder concentrically onto the sieve. In no case did we observe flocking, in the sense of an extended region of particles all aligned and moving in the same direction.

III. PROPAGATING WAVES

We observe a propagating compression wave instability for dense collections of fluidized rods. In Fig. 1 a time series of binary images, each separated by 0.09 s, depicts an example propagating compression wave for a system at 64% packing fraction. The red arc moves at constant velocity 28 cm/s, ahead of the wavefront, and serves as a guide to the eye. Since the rods are white and the background is dark, the compressed region at the front of the wave is brighter than the trailing rarefaction zone. In Fig. 1 this effect is accentuated, so that the density wave is more visually apparent, by thresholding the grayscale to black and white with a cutoff that increases the footprint of rods that are close together. For later quantitative analysis, a different cutoff is used such that all rods have close the same footprint. An example video clip is available on-line [37]. We emphasize that this phenomenon is unique to rods; we do not observe compression waves for spheres.

Note that the waves propagate through the medium without regard to any local or long-range ordering. As seen in the still photos of Fig. 1, the particles point in all directions with respect to the wavefront. And as seen in the videos, e.g. [37], the waves travel much faster than the particles move or reorient. Therefore successive waves often pass through the same region, but traveling in a different direction. Furthermore, they generally move straight across the entire sample, without seeming to scatter or refract from small regions with different local ordering.

To get an estimate for the wavespeed without any detailed processing, we look at spacetime plots of a single

line of pixels extracted from the video data, as shown in Fig. 2. The waves are visible on the spacetime plot as diagonal lines. From the slopes of these lines, we obtain a range of wavespeeds from 10 to 30 cm/s, in agreement with the moving arc in Fig. 1. From position-versus-time data for the individual rods, we calculate the root-mean-square particle speed of ∼1 cm/s. Thus, the waves move an order of magnitude faster than the particles themselves and an order of magnitude slower than the fluidizing airflow. This is similar to what has been observed for collective motion of bacteria in which the collective behavior is an order of magnitude faster than the individual particle speeds [20]. However, both a hydrodynamic theory of particles adsorbed on a substrate [38] as well as a microscopic theory of self-propelling rods [36] predict that propagating waves in those systems have a speed c equal to v_{rms}.

Predictions of waves typically require that long-range order or a dynamic broken symmetry state be present in the system. By eye, neither appears to develop for our systems. The propagation of the compression waves could disrupt the local ordering and any correlated motion developing between neighboring particles. Although there is no long-range order, localized domains of nematic ordering are observed and the particles in these regions tend to move in the same direction in a bulk sense. To quantify the extent of these local domains, we calculate the ensemble- and time-averaged orientational order parameter $\langle|e^{in\theta}|\rangle$ for $n = 2, 3, 4$. For a fixed packing fraction and airflow, we vary the neighborhood size over the which the ensemble average of orientations is taken. The neighborhood is a square subregion with side lengths $l \times l$. The result for a system at 64% packing fraction is shown in Fig. 3 where the subregion side length has been scaled by the rod length. If a system possesses an n-fold symmetry within the subregion, the quantity will be equal to 1. The results show that there is substantial nematic (n=2) local ordering with values of the order parameter ranging from 0.6 to 0.7 in a neighborhood of two particle lengths, indicating the tendency for neighboring rods to align along their long axes; the values for 3- and 4-fold symmetry are also appreciable. The quantity decays to approximately 0.1 when we average over the entire system. A fit to an exponential yields a $1/e$ correlation length of approximately 8 particle lengths, indicating medium-range order intermediate between particle size and system size.

IV. NUMBER FLUCTUATIONS

One interesting consequence of the propagating waves moving much faster than the individual rods is that compressed and dilute regions are larger than the particle size. Such persistent fluctuations in the density suggest the presence of anomalously large fluctuations in the local number density for these systems, which we now calculate. For a thermal system, the quantity $\Delta N/\sqrt{\langle N\rangle}$,

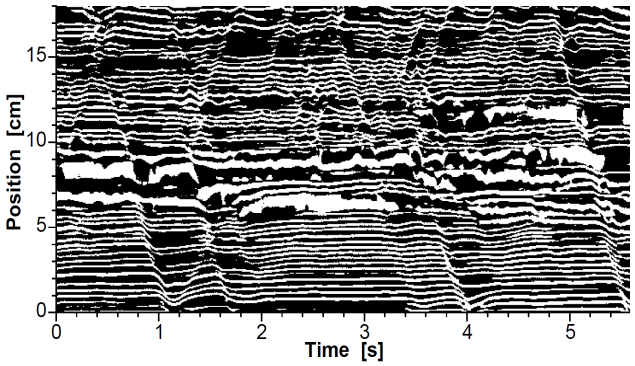

FIG. 2: Spacetime plot of a line of pixels taken from a video of air-fluidized rods as specified in Section II.

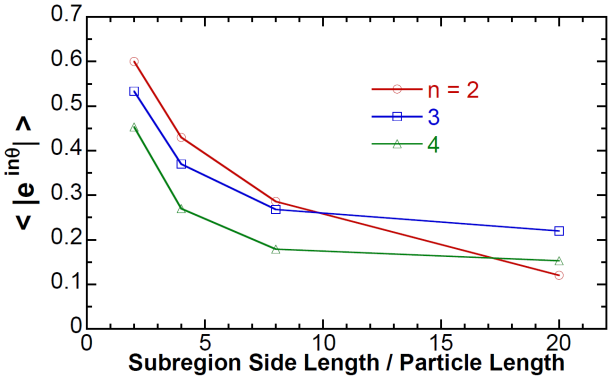

FIG. 3: (Color online) Time- and ensemble-averaged orientational order parameter $\langle|e^{in\theta}|\rangle$ for n= 2, 3, 4 for a system of air-fluidized rods at 64% packing fraction. The ensemble average is taken over all particle orientations within a square subregion with side lengths $l \times l$. The order parameter is plotted against this side length scaled by the rod length.

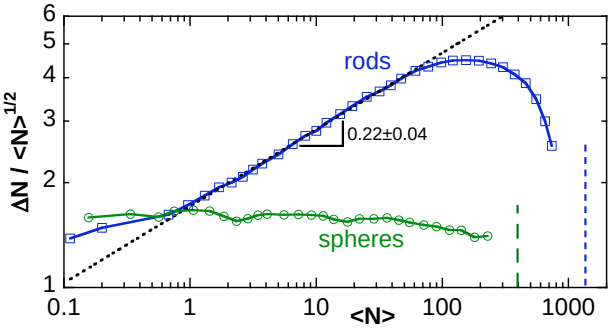

FIG. 4: (Color online) Magnitude of number fluctuations normalized by $\sqrt{\langle N\rangle}$ versus average number of particles in a subregion of the system. The circles are for a bidisperse collection of spheres. The squares are for a collection of rods. Both systems occupy 64% areal packing fraction and are fluidized at 220 cm/s. The vertical dashed lines correspond to the total number of particles in each system: 1353 rods and 400 spheres. The dashed line is a power-law fit, which corresponds to $\Delta N \sim \langle N\rangle^{0.72\pm0.04}$.

where $\langle N \rangle$ is the mean number of particles in a subregion and ΔN is the standard deviation, should be a constant. Thus, thermal behavior will be characterized by a horizontal line on a plot of $\Delta N/\sqrt{\langle N \rangle}$ versus $\langle N \rangle$, whereas so-called giant number fluctuations will be characterized by a non-zero slope and a magnitude larger than one.

To quantify number fluctuations, we take a 10-minute video of the system at a given packing fraction and airflow. We select a square subregion of interest with side length l and count the number of particles within that region for each frame. From this time series, we calculate the average $\langle N \rangle$ and the standard deviation ΔN. We then repeat this procedure for systematically larger regions of interest, ranging from a single pixel up to roughly half of the system size.

Results for a system at 64% packing fraction, fluidized at 220 cm/s, are shown in Figure 4 as a plot of $\Delta N/\sqrt{\langle N \rangle}$ versus $\langle N \rangle$ for each subregion. The number fluctuations for bidisperse spheres show ordinary behavior, with $\Delta N/\sqrt{\langle N \rangle} \approx 1.5$ being constant over the entire range of subregion sizes. Rods, however, show number fluctuations with both an exponent and magnitude larger than thermal expectations, indicating giant fluctuations in local number density. The large $\langle N \rangle$ fall-off is a finite size effect; the vertical dashed lines in Fig. 4 indicate the total number of particles in each system. At its maximum prior to this fall-off, the fluctuations in local number density of the rods are larger than those for spheres by more than a factor of 3. By fitting a power law to the rod data, we find that number fluctuations for the rods scale as $\Delta N \sim \langle N \rangle^{0.72 \pm 0.04}$.

Although the maximum in the number fluctuations is due to finite size effects, it serves as a useful benchmark to quantify the spatial extent of local number fluctuations. We accomplish this by converting the value of ΔN into an effective range of packing fractions. The value of $N + \Delta N$ at the maximum corresponds to a range of packing fractions $\phi \sim 64\% \pm 20\%$. Thus, as the wave propagates through the system, particles are compressed by the front up to 84% while the rarefaction zones are diluted to approximately 44%.

Figure 4 is strikingly similar to the number fluctuations obtained for rods fluidized by vertical vibrations [13]. In that experiment though, the large voids responsible for giant number fluctuations persisted for very long times, indicated by a logarithmic decay in the local density autocorrelation function. In our system, the density autocorrelation function decays to oscillations about zero within a few seconds. These two systems exhibit qualitatively similar giant number fluctuations, though caused by different mechanisms. The common factor between the two systems is that the rods self-propel at low densities.

V. WAVES AND DENSITY

Propagating waves have been predicted for collections of self-propelling particles interacting via volume exclusion with no emergent broken-symmetry state [36], as well as more generally for particles adsorbed on a surface in a fluid background [38]. In order to facilitate a theoretical description of our observations and understand the relative roles of particle shape and self-propelling, we must know how wavespeed and particle speed change with packing fraction and airflow. We do this by calculating a dynamic structure factor in subsection V A. We repeat the analysis for systems at different packing fractions and airflows in subsection V B. Lastly, in subsection V C, we map out the phase behavior of the rods.

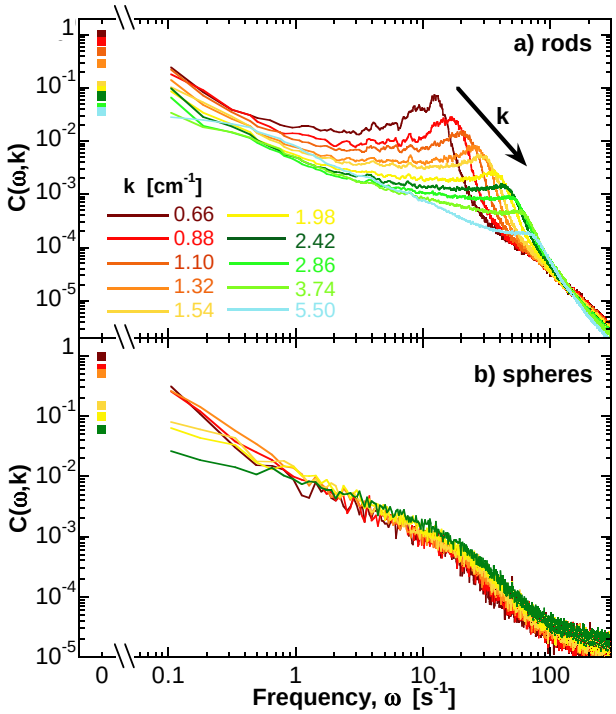

FIG. 5: (Color online) Spatiotemporal power spectrum of the density $C(\omega, k)$ for a) a collection of rods and b) a collection of bidisperse spheres, both occupying 64% packing fraction. Each curve corresponds to a different wave-vector value as shown by the color legend in (a). The DC-component for each curve is plotted to the left of the axis break. For the rods, note that for increasing k the peak near $\omega = 10$/s shifts to the right.

A. Density Power Spectrum

In this subsection, we obtain more detailed quantitative information about the waves by calculating the spatiotemporal power spectrum $C(\omega, |k|)$ of the density $\rho(x, y, t)$, where ω is frequency and $|k|$ is wave-vector. Since we cannot track all the particles at high densities, we simply use the 0-255 grayscale pixel values directly from the video data. As discussed above for Fig. 1, this may be taken as a proxy for the local density. This assumption cannot be tested without actually tracking all the rods, but we note (a) that the power spectra are es-

sentially the same if the video images are first thresholded to binary, and (b) that the resulting wave speeds agree well with expectations based on rough measurements like those in Figs. 1 and 2. Using LabVIEW's Vision package, we first obtain the spatial Fourier transform of each frame in the video. Because there is no long-range order, the spatial Fourier transform of the rods data shows two rings at $|k| \simeq 4.96$ cm^{-1} and 26.2 cm^{-1}, corresponding to the long and short dimensions of the rod. The annuli are isotropic with respect to the polar angle indicating that there is no long-range order in the system. We next extract the time-traces for all pixel values within an annulus at fixed $|k|$. We then calculate the temporal power spectrum for each pixel time-trace at fixed $|k|$ and average over all pixels to obtain the spatiotemporal power spectrum $C(\omega, |k|)$. The magnitude of the power spectrum as both ω and $|k| \to 0$ is simply the sum of the grayscale values of each frame in the video averaged over time. We normalize the power spectrum magnitude by this quantity so that the rods and spheres data can be more directly compared.

Slices of $C(\omega, |k|)$ for fixed $|k|$ are plotted versus ω in Fig. 5(a) for rods and 5(b) for spheres, both at 64% projected area fraction. The range of wave-vectors shown correspond to one-fourth the system size to approximately one particle length. The salient feature of $C(\omega, |k|)$ in Fig. 5(a) is a series of peaks, that shift to higher frequencies at increasing wave-vectors and hence that indicate a traveling excitation. For larger wave-vectors outside of the hydrodynamic limit, the peaks become less pronounced and roll over to an inflection. In contrast, the same analysis for spheres in Fig. 5(b) shows no such peaks and hence the absence of ballistic density waves.

By plotting the location of peak frequency versus $|k|$, we can construct the dispersion relationship for the waves, as shown by the symbols in Fig. 6. On this same figure, we also superpose a colorized contour plot of $C(\omega, |k|)$. In the limit of small wavevector and frequency, the dispersion relation is linear and we may therefore extract a wave speed $c = \omega/|k|$ from the slope. For this particular example, $c = 20.8$ cm/s. This is consistent with the video data which show the waves propagating across the system in 1-2 seconds as well as the value obtained from spacetime plots. Again, we note that the wave speed is an order of magnitude larger than the rms speed of the particles, $v_{rms} \sim 1$ cm/s, and an order of magnitude smaller than the fluidizing airflow ~ 200 cm/s.

B. Wavespeed

Now we may measure the wavespeed as a function of both packing fraction and airspeed, using the spatiotemporal power spectra as illustrated in the examples of Figs. 5-6. For comparison, we also use particle tracking to measure the rms speeds parallel and perpendicular to the long axis of the rods. The results are displayed in

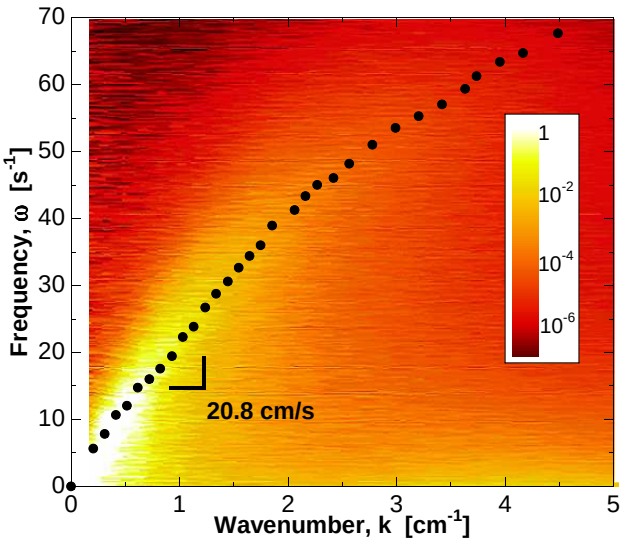

FIG. 6: (Color online) Contour plot of the spatiotemporal power spectrum of the density for rods occupying 64% packing fraction and fluidized at 220 cm/s. The power spectrum amplitude is given in the color legend. The peaks found in Fig. 5 are plotted as solid circles, and constitute the dispersion relation. The slope of the linear region is the wave speed, $c = 20.8$ cm/s.

the four plots of Fig. 7. At fixed air speed, the wave speed increases slightly as we increase the packing fraction of the system as seen in Fig. 7(a). The increase appears to be roughly linear, although the dynamic range of our data is limited. This linear trend is seen for several other fixed airflows that we analyzed. By contrast, if we fix the packing fraction and increase the fluidizing airflow, the wavespeed shows no dependence on airflow, Fig. 7(b). From Fig. 7(c), we see that the particle speeds increase slightly with increasing density; from (d), we see a similar increase in particle speed with increasing airflow except at the highest airflows. For high airflows, out-of-plane motion dominates and in-plane motion slows down. For most densities, the speed parallel to the rod axis is slightly larger than the transverse speed, although the effect is smaller than that observed for dilute systems [16].

For all densities and airspeeds analyzed, the wavespeed remains an order of magnitude larger than the particle speed and the components of the particle speed remain nearly equal. This indicates that when propagating waves are present, the particles velocities are no longer anistropic. This is demonstrated more powerfully in Fig. 8, where we extend the particle rms speed measurements to lower packing fractions. For this particular density and airflow, waves are no longer observed below 50% packing fraction. And below this packing fraction, we see that the parallel and perpendicular particle speeds become appreciably different. Thus, we conclude that speed anisotropy and waves appear exclusive of one another.

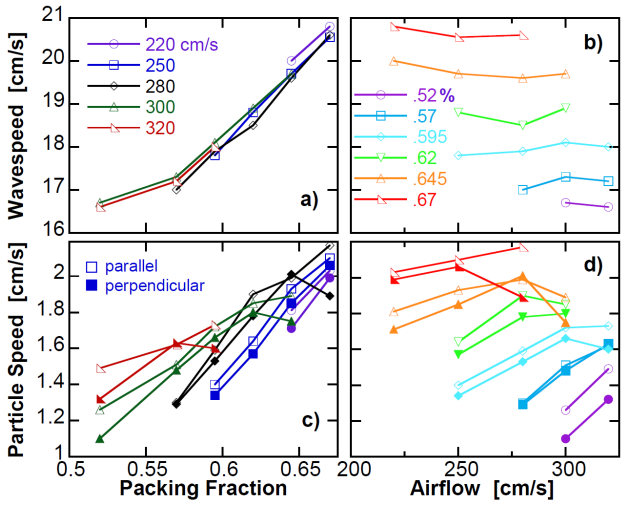

FIG. 7: (Color online) Wavespeed as a function of a) packing fraction and b) airflow and root-mean-square parallel (open symbols) and perpendicular (closed symbols) particle speeds as a function of c) packing fraction and d) airflow.

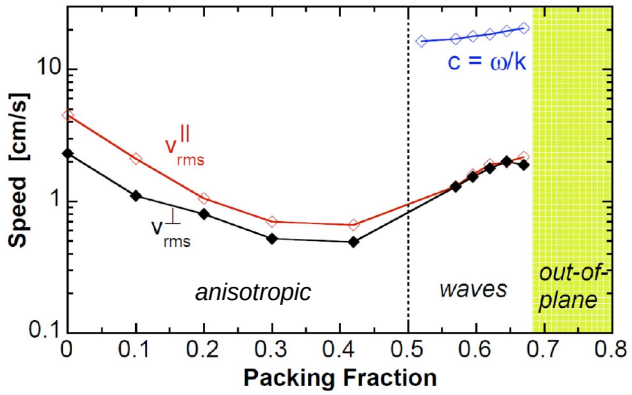

FIG. 8: (Color online) Wavespeed ($c = \omega/k$) and root-mean-square parallel ($v^{\parallel}_{\rm rms}$) and perpendicular ($v^{\perp}_{\rm rms}$) particle speeds as a function of packing fraction for rods fluidized at 280 cm/s. The shaded region is where out-of-plane motion becomes substantial.

C. Phase Behavior

Since we observed that speed anisotropy and waves are mutually exclusive, we want to determine the conditions for which a system of rods exhibits each phenomenon. Here, we qualitatively map out the phase behavior of fluidized rods as a function of packing fraction and fluidizing airflow, Fig. 9. We explored a range of densities from a single particle up to 75% packing fraction and fluidization speeds from 150 cm/s to 500 cm/s. We first place the desired number of rods into the system with no air flow. We then turn the airspeed to 150 cm/s. We increase the airspeed slowly by increments of roughly 10 cm/s. After each increase in the airflow, we wait one minute to ensure the system has reached a steady state and then characterize the behavior observed before increasing airflow once more. There are strong particle-wall interactions that cause the rods to cluster in the center of the system at low densities. Thus, the exact shape of the phase boundaries system-size-dependent. As such, we show a phase diagram for the full system size (diameter 28.6 cm) in Fig. 9(a) as well as the system size used in Ref. [16] (diameter 17 cm) in Fig. 9(b). Because packing fraction is ill-defined unless the particles are uniformly distributed across the system, we denote the packing fraction above which the rods are uniformly dense as a vertical dashed line in both Figs. 9(a) and (b).

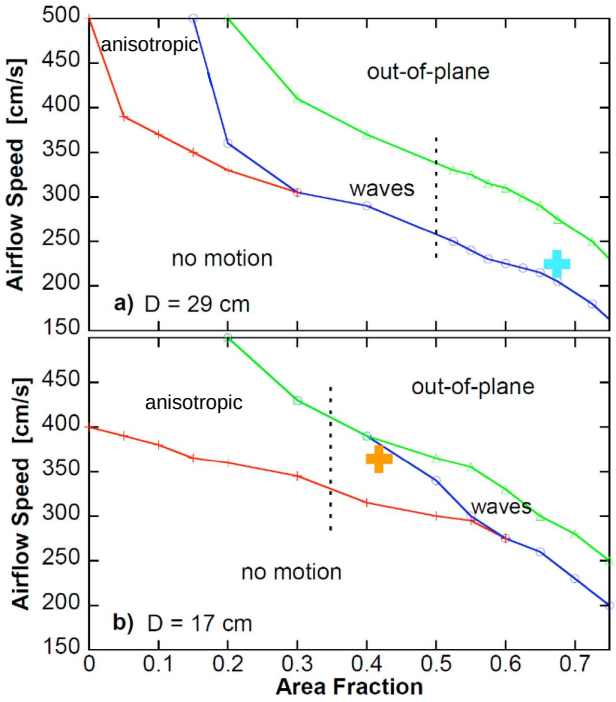

FIG. 9: (Color online) Behavior of fluidized rods as a function of fluidizing airflow and packing fraction. The diagram in a) is for a large system with diameter 29 cm; b) is for a smaller system with diameter 14 cm. The solid cross in (a) represents conditions for the analysis of Sections VA. The solid cross in (b) represents the conditions for the experiment of Ref. [16]. The vertical dashed line in both plots corresponds to the density above which the rods are uniformly distributed about the system.

For all packing fractions, there is a threshold airflow below which the rods do not move. This is the lower boundary of the phase diagrams shown in Fig. 9. Conversely, above some airflow, the rods gain enough energy to lose contact with the substrate and overlap one another out-of-plane. This marks the upper boundary of the phase diagrams which is determined by when we first observe two rods overlapping. Within these boundaries, we observe two distinct behaviors depending on both packing fraction and airflow. For dilute systems, the rod densities are spatially uniform and the speeds are anistropic with very little out-of-plane motion. The

experimental conditions for our previous work [16] are shown as the solid orange cross in Fig. 9(b). As density is increased, there emerges an instability for compression waves to propagate. The onset of waves is chosen to be when ripples first appear to the eye.

VI. CONCLUSION

In summary we have investigated the behavior of dense collections of rods fluidized by an upflow of air. At low packing densities the particle speeds are anisotropic with respect to the long and short axes of the rods, and so we had hoped to observe swarming or flocking behavior at high densities. Instead, we found that the anisotropy vanished with the simultaneous development of ballistic density waves and giant number fluctuations. We quantified the latter in terms of the standard deviation of the number of rods in a given subregion, versus subregion size. And we quantified the waves in terms of a spatiotemporal power spectrum. From the position of peaks in this function, we extracted a dispersion relationship and hence the wavespeed, which turned out to be much faster than the particle speed and much slower than the fluidizing air speed. And finally we mapped out a phase diagram for the general state of behavior as a function of rod packing density and of the fluidizing air speed.

The transition between a phase with anisotropic velocities and a phase with giant number fluctuations and waves is a striking feature, though not yet understood. In fact we have no firm explanation for why density waves can even exist for air fluidized rods but not for fluidized spheres; furthermore we are unaware of density waves for a system of vibrofluidized rods. One possible mechanism is that the local particle density affects the average upflow of air or the way turbulent wakes are shed; however, such a mechanism ought to similarly cause density waves for the spheres. Furthermore, the local air speed is set by the pressure drop across the sieve, which is much greater than the pressure drop across the rods; hence the upflow is insensitive to particle density. Another possibility is that advection plays a role, according to the Peclet number [20] given by the ratio VL/D of advection to diffusion. Here $V \approx 1$ cm/s is the particle speed, $L \approx 1$ cm is the particle length, and $D \approx 0.1$ cm^2/s is the diffusion constant found from the linear regime of the particle mean square displacements obtained by individually tracking the rods [16]. This gives a Peclet number of $VL/D \approx 10$, suggesting that advection could play a role. Yet another possible explanation would entail an inertial argument in which the rods attempt to move preferentially along their long axis but are thwarted by the reduced free area available to them. Thus, during a collision with another rod, there is an additional transfer of momentum that pushes the second rod into a third rod, giving rise to a cascade of collisions that result in a propagating wave. This effect could be coupled with dynamic clustering due to inelasticity, as invoked to explain giant number fluctuations in vibro- and electro-fluidized spheres [39]. However, none of these explanations accounts well for the absence of waves for our system of air-fluidized spheres. We suspect that the orientational order captured in Fig. 3, though subtle, must play an important role.

Acknowledgments

We thank Aparna Baskaran for helpful discussions on particle and wave speeds, and we thank John Toner for helpful discussions on ordering and giant number fluctuations. This work was supported by the NSF through grant DMR-0704147.

[1] R. Brown and J. Richards, *Principles of Powder Mechanics: Essays on the Packing and Flow of Powders and Bulk Solids* (Pergamon Press, Oxford, 1970).
[2] R. M. Nedderman, *Statics and kinematics of granular materials* (Cambridge University Press, NY, 1992).
[3] H. M. Jaeger, S. R. Nagel, and R. P. Behringer, Rev. Mod. Phys. **68**, 1259 (1996).
[4] R. P. Ojha, P. A. Lemieux, P. K. Dixon, A. J. Liu, and D. J. Durian, Nature **427**, 521 (2004).
[5] A. R. Abate and D. J. Durian, Phys. Rev. E **74**, 031308 (2006).
[6] A. R. Abate and D. J. Durian, Phys. Rev. Lett. **101**, 245701 (2008).
[7] D. L. Blair, T. Neicu, and A. Kudrolli, Phys. Rev. E **67**, 031303 (2003).
[8] J. Atwell and J. S. Olafsen, Phys. Rev. E **71**, 062301 (2005).
[9] J. Galanis, D. Harries, D. L. Sackett, W. Losert, and R. Nossal, Phys. Rev. Lett. **96**, 028002 (2006).
[10] V. Narayan, N. Menon, and S. Ramaswamy, J. Stat. Mech. **2006**, P01005 (2006).
[11] I. S. Aranson, D. Volfson, and L. S. Tsimring, Phys. Rev. E **75**, 051301 (2007).
[12] Z. E. Dell and S. V. Franklin, J. Stat. Mech. **2009**, P09010 (2009).
[13] V. Narayan, S. Ramaswamy, and N. Menon, Science **317**, 105 (2007).
[14] A. Kudrolli, G. Lumay, D. Volfson, and L. S. Tsimring, Phys. Rev. Lett. **100**, 058001 (2008).
[15] A. R. Abate and D. J. Durian, Phys. Rev. E **72**, 031305 (2005).
[16] L. J. Daniels, Y. Park, T. C. Lubensky, and D. J. Durian, Phys. Rev. E **79**, 041301 (2009).
[17] J. Toner, Y. H. Tu, and S. Ramaswamy, Ann. Phys. **318**, 170 (2005).
[18] S. Ramaswamy, Ann. Rev. Cond. Matt. Phys. **1**, 323 (2010).
[19] U. Börner, A. Deutsch, H. Reichenbach, and M. Bär,

Phys. Rev. Lett. **89**, 078101 (2002).
[20] C. Dombrowski, L. Cisneros, S. Chatkaew, R. E. Goldstein, and J. O. Kessler, Phys. Rev. Lett. **93**, 098103 (2004).
[21] O. A. Igoshin, R. Welch, D. Kaiser, and G. Oster, Proc. Nat. Acad. Sci. **101**, 4256 (2004).
[22] R. Welch and D. Kaiser, Proc. Nat. Acad. Sci. **98**, 14907 (2001).
[23] K. H. Koltes, Marine Biol. **78**, 113 (1983).
[24] J. Buhl, D. J. T. Sumpter, I. D. Couzin, J. J. Hale, E. Despland, E. R. Miller, and S. J. Simpson, Science **312**, 1402 (2006).
[25] M. Ballerini, N. Cabibbo, R. Candelier, A. Cavagna, E. Cisbani, I. Giardina, A. Orlandi, G. Parisi, A. Procaccini, M. Viale, et al., Animal Behaviour **76**, 201 (2008).
[26] P. F. Major and L. M. Dill, Behav. Ecol. and Sociobiol. **4**, 111 (1978).
[27] D. Helbing, Rev. Mod. Phys. **73**, 1067 (2001).
[28] A. John, A. Schadschneider, D. Chowdhury, and K. Nishinari, Phys. Rev. Lett. **102**, 108001 (2009).
[29] T. Vicsek, A. Czirok, E. Ben-Jacob, I. Cohen, and O. Shochet, Phys. Rev. Lett. **75**, 1226 (1995).
[30] J. Toner and Y. Tu, Phys. Rev. Lett. **75**, 4326 (1995).
[31] J. Toner and Y. Tu, Phys. Rev. E **58**, 4828 (1998).
[32] Y. Tu, J. Toner, and M. Ulm, Phys. Rev. Lett. **80**, 4819 (1998).
[33] R. A. Simha and S. Ramaswamy, Phys. Rev. Lett. **89**, 058101 (2002).
[34] S. Ramaswamy, R. Simha, and J. Toner, Europhys. Lett. **62**, 196 (2003).
[35] H. Chate, F. Ginelli, and R. Montagne, Phys. Rev. Lett. **96**, 180602 (2006).
[36] A. Baskaran and M. C. Marchetti, Phys. Rev. E **77**, 011920 (2008).
[37] EPAPS number *tbd*. Example real-time video clip demonstrating ballistic density waves. The areal packing fraction is 64%, the same as in Figure 1 of the main text. The air speed is 250 cm/s, which is a little faster than that in Figure 1.
[38] S. Ramaswamy and G. F. Mazenko, Phys. Rev. A **26**, 1735 (1982).
[39] I. S. Aranson, A. Snezhko, J. S. Olafsen, and J. S. Urbach, Science **320**, 612 (2008).